

A simple finite element model of diffusion, finite deformation, plasticity and fracture in lithium ion insertion electrode materials

This content has been downloaded from IOPscience. Please scroll down to see the full text.

2012 Modelling Simul. Mater. Sci. Eng. 20 045004

(<http://iopscience.iop.org/0965-0393/20/4/045004>)

View [the table of contents for this issue](#), or go to the [journal homepage](#) for more

Download details:

IP Address: 134.225.1.226

This content was downloaded on 29/12/2014 at 12:51

Please note that [terms and conditions apply](#).

A simple finite element model of diffusion, finite deformation, plasticity and fracture in lithium ion insertion electrode materials

A F Bower¹ and P R Guduru

School of Engineering, Brown University, Providence, RI 02912, USA

Received 28 October 2011, in final form 28 February 2012

Published 2 April 2012

Online at stacks.iop.org/MSMSE/20/045004

E-mail: Allan.Bower@brown.edu and Pradeep.Guduru@Brown.edu

Abstract

We describe a finite element method for modeling deformation, diffusion, fracture and electrochemical reactions in materials used as lithium ion insertion electrodes. With a view to modeling high-capacity composite electrode materials such as silicon or tin, the model accounts for finite deformations and plastic flow, and models the evolving electrochemical boundary conditions resulting from the creation of new fracture surfaces using a cohesive zone. In addition, a simple mixed element is used to account for the driving force for diffusion arising from stress gradients. In this approach, the equations for diffusion and deformation are fully coupled, and can be integrated using a stable implicit time-stepping scheme. The method is illustrated by modeling plastic flow and fracture during cyclic lithiation of a thin-film Si electrode and a simple model of a battery microstructure.

(Some figures may appear in colour only in the online journal)

1. Introduction

There is great interest in improving the performance of lithium ion batteries, particularly for applications such as electric vehicles and grid storage, where battery materials must tolerate large numbers of cycles at high rates of charge and discharge. The current generation of Li ion batteries generally use a carbon-based anode, and a variety of materials for the cathode, including lithium cobalt oxide, lithium manganese oxide and lithium iron phosphate. All electrode materials experience volume changes as lithium is inserted or removed during operation of the battery. The stresses generated by these volume changes cause electrodes to fail by fatigue or fracture under repeated cycling [1]. Mechanical failures are a particular

¹ Author to whom any correspondence should be addressed.

concern in high-capacity electrode materials such as silicon or tin, which have the potential to increase the specific energy density of a battery substantially, but which experience extreme changes in volume during lithiation (as much as 300% for Si). There is hope that failures can be minimized or eliminated by designing damage-tolerant electrode microstructures, and a variety of composite electrode materials are being explored with this in mind.

The ability to model damage evolution in representative battery microstructures would aid the design process significantly. This has motivated a number of recent models of stress evolution, diffusion and fracture in representative battery microstructures. These include detailed models of stress evolution in a single particle [2–9], cohesive zone models of fracture in particles during lithiation, [10], nanowires [11] or thin films [12, 13], as well as more detailed models which consider collective behavior of an entire microstructure [14–19]. To make progress, these models all introduce various approximations: in some cases the microstructure is idealized with a simple spherically symmetric geometry; the material is usually assumed to be elastic; models are restricted to small strains, or simplified boundary conditions are adopted.

A full analysis of a complex battery microstructure can only be accomplished using numerical methods (the finite element method is the most straightforward approach). This poses several challenges. Firstly, it is necessary to solve the coupled field equations of mechanical equilibrium and Li diffusion, accounting for the effects of stress on diffusion. The field equations may be nonlinear even if the material deforms reversibly, because of the large volume changes that occur during lithiation. In addition, the large volume changes must be treated carefully in a finite element implementation to avoid locking. Some electrode materials also deform plastically [20, 21]. It is of particular interest to model fracture and fatigue, which can be treated using cohesive zone models. Standard cohesive zone models must be extended to account for Li insertion through the faces of open cracks. Finally, finite element methods must treat the boundary conditions associated with Li insertion at particle surfaces.

In this paper we describe a simple and robust finite element implementation that meets these requirements. In the next section, we review the constitutive equations developed to describe finite deformation, plasticity, Li diffusion and electrochemical reactions in an electrode, and augment these with a simple cohesive zone model that can approximate the evolving boundary conditions resulting from the creation of new fracture surfaces. Section 3 then describes an efficient finite element implementation of the constitutive law and governing equations: a mixed formulation, in which the chemical potential is a degree of freedom, enables the diffusion and equilibrium equations to be solved simultaneously using a robust and efficient fully implicit time integration scheme, while a small modification of the B-bar method is used to eliminate locking. Finally, section 4 describes several representative applications of the finite element model, such as modeling plastic flow and fracture during lithiation of thin films and spherical particles.

2. Governing equations

A representative boundary value problem is shown in figure 1. We consider a solid particle in the electrode, whose surface contacts an electrolyte. An actual electrode microstructure consists of a large number of such particles, which are held together by a binder, but focusing on a single particle is sufficient for our purposes.

We suppose that at time $t = 0$ the particle is stress free, contains a molar density ρ_0 of electrode atoms and contains no lithium. It occupies a volume V_0 and has surface S_0 . It is convenient to take this state as the reference configuration. During operation, a flux of Li atoms is inserted into the particle by the electrochemical reaction occurring at the particle

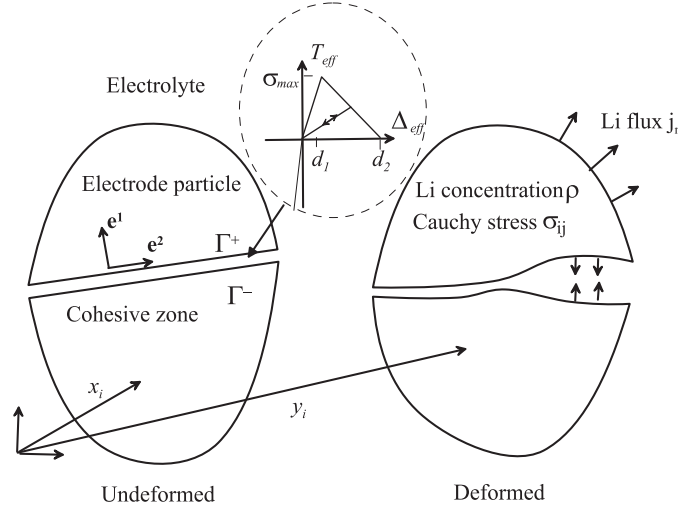


Figure 1. Idealized model of deformation and fracture in a solid electrode particle caused by Li insertion and diffusion. The traction–separation relation for the cohesive zone model is shown in the inset.

surface. As a result, Li atoms diffuse through the particle, causing it to change its shape. The concentration of Li atoms per unit reference volume will be denoted by ρ_{Li} , and we also introduce the Li fraction $c = \rho_{\text{Li}}/\rho_0$. The deformation causes a material particle that is located at position x_i in the reference configuration to move to a new position y_i in the deformed solid. The deformation induces stress in the solid, which will be characterized by the Cauchy (‘true’) stress σ_{ij} . The stress may cause plastic flow in the particle, and may also cause the particle to fracture along a set of **pre-determined planes** Γ . In the following, we will summarize the equations governing deformation in the bulk particle; Li diffusion, material separation and the Li insertion process resulting from the electrochemical reaction at the particle surface and on open crack faces.

2.1. Deformation and diffusion in the bulk electrode

To quantify the deformation of the particle, we introduce the usual measures of deformation gradient, its Jacobian and the velocity gradient

$$F_{ij} = \frac{\partial y_i}{\partial x_j}, \quad J = \det(F_{ij}), \quad L_{ij} = \frac{\partial \dot{y}_i}{\partial y_j} = \dot{F}_{ik} F_{kj}^{-1}. \quad (1)$$

Shape changes occur as a result of three distinct processes: (i) an irreversible plastic deformation of the underlying electrode material, (ii) **a shape change caused by inserting Li into the electrode** and (iii) a reversible elastic deformation. Each of these can be characterized by a separate deformation gradient, which together produce the overall shape change

$$F_{ij} = F_{ik}^e F_{kl}^c F_{lj}^p. \quad (2)$$

For simplicity, we will assume that the **shape changes caused by inserting Li** consist of an **isotropic volumetric expansion**

$$F_{ij}^c = \beta(c)^{1/3} \delta_{ij}. \quad (3)$$

This is a good approximation of the behavior of Si, but many electrode materials (including graphitic electrodes) experience an **anisotropic shape change**. It would be straightforward to

generalize the analysis to account for anisotropy, but we will not attempt to do so here to avoid unnecessary algebra. The velocity gradient can also be decomposed into three contributions

$$\begin{aligned} L_{ij} &= L_{ij}^e + L_{ij}^c + L_{ij}^p, \\ L_{ij}^e &= \dot{F}_{ik}^e F_{kj}^{e-1}, \quad L_{ij}^c = F_{in}^e \dot{F}_{nl}^c F_{lk}^{c-1} F_{kj}^{e-1} = \frac{1}{\beta} \frac{\partial \beta}{\partial c} \dot{c}, \quad L_{ij}^p = F_{in}^e F_{nm}^c \dot{F}_{mr}^p F_{rl}^{p-1} F_{lk}^{c-1} F_{kj}^{e-1}. \end{aligned} \quad (4)$$

Constitutive equations must relate L_{ij}^e and L_{ij}^p to the stress in the particle. We adopt the constitutive model proposed in [22] for this purpose. The stress is related to the elastic strain by

$$J F_{ik}^{e-1} \sigma_{kl} F_{jl}^{e-1} = C_{ijkl}(c) E_{kl}^e \quad E_{ij}^e = (F_{ki}^e F_{kj}^e - \delta_{ij})/2 \quad (5)$$

where C_{ijkl} are the elastic constants for the electrode in the reference configuration. It is important to interpret equation (5) carefully. Firstly, a linear relationship between stress and elastic Lagrange strain is valid only if elastic distortions are infinitesimal. This is a reasonable approximation for most practical electrode materials, but may not be the case in some polymeric electrode materials. Secondly, note that the elastic constants C_{ijkl} relate the *nominal* stress to the elastic Lagrange strain (these are thermodynamic conjugate variables, as shown in [22]). Consequently, if the moduli C_{ijkl} are constant, the true stress–true strain relation for the material softens as it is lithiated. Other descriptions of the elastic response are possible, but our choice is thermodynamically consistent, and is convenient for numerical computations.

The plastic strain rate is related to the stress by a simple isotropic viscoplastic constitutive law

$$L_{ij}^p = \dot{\epsilon}_0 \left\langle \frac{\tau_e}{\sigma_0(c)} - 1 \right\rangle^m \frac{3}{2} \frac{\tau_{ij}^D}{\tau_e}, \quad \tau_{ij}^D = \tau_{ij} - \tau_{kk} \delta_{ij} \quad \tau_e = \sqrt{3 \tau_{ij}^D \tau_{ij}^D / 2} \quad (6)$$

where $\langle x \rangle = x$, $x > 0$; $\langle x \rangle = 0$, $x < 0$, $\tau_{ij} = J \sigma_{ij}$ is the Kirchhoff stress. In subsequent calculations, it is convenient to re-write equations (5) and (6) in rate form: a standard calculation shows that (provided the elastic strains are small), the rate of change of Kirchhoff stress components are

$$\frac{d\tau_{ij}}{dt} = C_{ijkl}^e D_{kl}^e + W_{ik} \tau_{kj} - \tau_{ik} W_{kj} + \frac{\partial C_{ijkl}^e}{\partial c} \frac{\partial c}{\partial t} S_{klmn}^e \tau_{mn} \quad (7)$$

where $D_{ij}^e = (L_{ij}^e + L_{ji}^e)/2$, $W_{ij} = (L_{ij}^e - L_{ji}^e)/2$ and

$$C_{ijkl}^e = F_{ip}^e F_{jq}^e C_{pqrs} F_{kr}^e F_{ls}^e, \quad S_{ijkl}^e = C_{ijkl}^{e-1}. \quad (8)$$

Note that plastic spin has been taken to be zero in writing equations (6) and (7).

In this paper, we shall restrict our attention to the particular case of an elastically isotropic solid. This is appropriate for Si, but graphitic electrode materials are elastically anisotropic. It is straightforward to extend our results to account for anisotropy, but we avoid doing so to avoid algebraic complexity. The elastic properties of an isotropic solid can be characterized by two constants: here we use a generalized Young's modulus E (which is assumed to be a function of Li concentration), together with a generalized Poisson's ratio ν (which is assumed constant, for simplicity). We refer to 'generalized' elastic constants to emphasize that they relate material stress to elastic Lagrange strain in our constitutive model, and do not characterize the true stress–true strain relation. With these assumptions, equation (7) reduces to

$$\frac{d\tau_{ij}}{dt} = \frac{E}{1+\nu} \left\{ D_{ij}^e + \frac{\nu}{1-2\nu} D_{kk}^e \delta_{ij} \right\} + W_{ik} \tau_{kj} - \tau_{ik} W_{kj} + \frac{1}{E} \frac{\partial E}{\partial c} \frac{\partial c}{\partial t} \tau_{ij}. \quad (9)$$

Governing equations for the mechanical deformation are completed by the equilibrium equation for Cauchy stress $\partial \sigma_{ij} / \partial y_i = 0$ and boundary conditions $\sigma_{ij} n_j = 0$ on traction free surfaces.

Li diffusion through the bulk electrode is driven by a chemical potential

$$\mu = RT \log \left(\frac{\gamma c}{c_0} \right) - \frac{1}{2\rho_0} \frac{\partial S_{ijkl}}{\partial c} \tau_{ij} \tau_{kl} - \frac{\tau_{kk}}{3\rho_0} \frac{1}{\beta} \frac{\partial \beta}{\partial c} \quad (10)$$

where R is the gas constant, T is temperature, γ is the activity coefficient (which may depend on concentration) for Li in the stress free solid, and c_0 is a reference concentration. The molar flux of Li crossing unit reference area is related to the chemical potential by

$$j_i = - \frac{D\rho_0 c}{RT} \frac{\partial \mu}{\partial x_i} \quad (11)$$

where D is a temperature-dependent diffusion coefficient. Temperature gradients are neglected in our formulation, and so do not contribute to diffusion. The evolution equations for Li concentration are completed by the mass conservation relation

$$\rho_0 \frac{\partial c}{\partial t} + \frac{\partial j_i}{\partial x_i} = 0. \quad (12)$$

2.2. Electrochemical reactions

Li is inserted into the electrode as a consequence of electrochemical reactions taking place at the interface between the electrode and the surrounding electrolyte. A full treatment of a battery requires a model for transport and chemical reactions through the electrolyte, which will not be attempted here. To simplify computations, we assume that the electrical conductivity of the electrode is sufficiently large, and diffusion through the electrolyte is sufficiently fast, to maintain a constant electric potential in both the electrode and electrolyte. These are common assumptions in the electrochemical literature [23]. Under these conditions, charge is confined to the double layer at the electrode–electrolyte interface, and a uniform electric potential difference $\Delta\phi$ develops across the double layer at the surface. We take $\Delta\phi$ to be positive if the electrode has a higher electrical potential than the electrolyte. In our computations, we will assume that the system is loaded electrically by an external agency, which either draws a prescribed total current I from the electrode, or else maintains the potential difference $\Delta\phi$ at a prescribed value.

The electrochemical reaction at the surface of a Li ion insertion electrode is $\text{Li}^+ + \text{e}^- \rightarrow \text{Li}$. If an electric current I flows out of the electrode to an external circuit, the forward reaction occurs at the interface. The electrons associated with this current combine with Li^+ ions from the electrolyte at the electrode/electrolyte interface, and a flux of Li is inserted into the electrode surface.

If the electrode is left at open-circuit ($I = 0$) until it reaches mechanical and chemical equilibrium, the rates of forward and reverse reactions at the interface are equal, and the potential difference $\Delta\phi$ reaches the ‘rest potential’

$$\Delta\phi_0 = \frac{RT}{f} \left\{ \Theta(c) - \log \left(\frac{\gamma c}{c_0} \right) \right\} + \frac{1}{f} \left\{ \frac{1}{2\rho_0} \frac{\partial S_{ijkl}}{\partial c} \tau_{ij} \tau_{kl} + \frac{\tau_{kk}}{3\rho_0} \frac{1}{\beta} \frac{\partial \beta}{\partial c} \right\} \quad (13)$$

where f is the Faraday constant (the product of the magnitude of the electronic charge and the Avogadro constant), and $\Theta(c)$ is a function quantifying the relative rates of forward and reverse reactions at the interface under standard conditions (for an ideal reaction, $\Theta(c)$ is constant). The first term in equation (13) is the standard Nernst equation for a stress free electrode. The second term modifies the Nernst equation to account for the effects of stress on the chemical potential of Li in the electrode. This correction is discussed in more detail in [20, 22].

Under non-equilibrium conditions, the current flow from the electrode into the reaction layer is governed by the Butler–Volmer equation

$$i = i_0(c) \left\{ \exp \left(\frac{\alpha f (\Delta\phi - \Delta\phi_0)}{RT} \right) - \exp \left(- \frac{(1 - \alpha) f (\Delta\phi - \Delta\phi_0)}{RT} \right) \right\} \quad (14)$$

where i is the current density per unit reference area, $i_0(c)$ is the exchange current density (which represents the equal and opposite forward and reverse currents flowing across the interface at open-circuit equilibrium), and $0 < \alpha < 1$ is a phenomenological ‘symmetry factor’. The molar flux of Li flowing out of the electrode surface per unit area of reference surface follows as $j_n = j_i n_i = i/f$. For simplicity, we take i_0 to be constant in the simulations reported here, but in reality the exchange current density varies with concentration.

2.3. Fracture

We model fracture using a standard cohesive zone model, which permits material planes adjacent to a fracturing interface to separate, and uses a traction–separation law to model the resistance to crack nucleation and growth. Our main objective here is to extend this approach to account for Li transport across the interface. It is helpful to begin with a brief summary of the underlying processes.

We shall assume that Li flows freely across an undamaged interface or across the faces of a closed crack. If the two material surfaces adjacent to the interface separate under stress, the crack faces are exposed to the electrolyte. As a result, the electrochemical reaction described in the preceding section may take place at the crack surfaces, and Li may be inserted into each crack face. To model this process, we will assume that Li transport through an open crack is sufficiently fast so that the concentration of Li and the electrical potential of the electrolyte within the crack are equal to that of the bulk electrolyte. If the crack subsequently closes, the electrolyte is expelled from the crack and the electrochemical reaction at the crack surfaces ceases.

We quantify these processes as follows. The two material surfaces adjacent to a representative interface Γ are designated Γ^\pm . At each point on the interface, we introduce three unit vectors e_i^α , with e_i^1 the outward normal to Γ^- , and e_i^2, e_i^3 mutually perpendicular and in the plane of the interface. We then define the normal and tangential separation $\Delta_\alpha = e_i^\alpha (u_i^+ - u_i^-)$, and define $T_\alpha e_i^\alpha$ (with summation assumed on α) to be the nominal traction acting on Γ^- . The relative tangential motion of the two adjacent material surfaces is assumed to remain small, so that equal and opposite tractions act on the two coincident points on Γ^\pm throughout the deformation.

The tractions are related to the displacements using a history-dependent constitutive equation adapted from [24]. The traction–separation law is illustrated in figure 1. The tractions are related to the displacements by

$$\begin{aligned} T_1 &= k_0(1 - \Lambda)\Delta_1 + \xi \frac{d\Delta_1}{dt} - k_1 \langle -\Delta_1 \rangle, \\ T_2 &= \theta^2 k_0(1 - \Lambda)\Delta_2 + \xi \frac{d\Delta_2}{dt}, \quad T_3 = \theta^2 k_0(1 - \Lambda)\Delta_3 + \xi \frac{d\Delta_3}{dt} \end{aligned} \quad (15)$$

where k_1 is a large compressive stiffness that prevents the crack faces from overlapping, k_0 is the tensile stiffness of the undamaged interface, θ is a material parameter that controls the relative stiffness of the interface in shear and tension, ξ is a small fictitious viscosity introduced to improve numerical stability, and $0 < \Lambda < 1$ is a scalar measure of damage. The interface initially is undamaged with $\Lambda = 0$. To characterize damage evolution, we introduce the

effective interface separation and traction

$$\Delta_{\text{eff}} = \sqrt{\Delta_1^2 + \theta^2(\Delta_2^2 + \Delta_3^2)}, \quad T_{\text{eff}} = \sqrt{T_1^2 + (T_2^2 + T_3^2)/\theta^2}. \quad (16)$$

In addition, the interface strength is related to the damage by

$$T_0 = \sigma_{\text{max}}(1 - \Lambda)d_2/(d_2 - \Lambda(d_2 - d_1)) \quad (17)$$

where σ_{max} is the initial strength of the interface, $d_1 = \sigma_{\text{max}}/k_0$, and d_2 is the interface separation. Note that the work of separation for the interface is $\Phi = \sigma_{\text{max}}d_2/2$. The damage parameter then evolves according to

$$\frac{d\Lambda}{dt} = \begin{cases} 0, & T_{\text{eff}} < T_0 \\ \frac{d_1 d_2}{\Delta_{\text{eff}}^2(d_2 - d_1)} \left\langle \frac{d\Delta_{\text{eff}}}{dt} \right\rangle, & T_{\text{eff}} = T_0. \end{cases} \quad (18)$$

To account for Li insertion and removal through the faces of a crack, we must prescribe the flux j_n^\pm flowing out of each face of the crack. We set

$$j_n^\pm = j_{\text{elec}}^\pm + j_{\text{diff}}^\pm \quad (19)$$

where j_{elec}^\pm is the Li flux out of the crack faces from electrochemical reactions, and j_{diff}^\pm is the diffusion of Li out of each crack face to the other. The flux from electrochemical reactions is zero if the crack is closed, and increases until it reaches the flux associated with the Butler–Volmer equation (14) as the crack opens:

$$j_{\text{elec}}^\pm = \begin{cases} 0, & \Delta_1 < d_1 \\ (i/f)(\Delta_1 - d_1)/(d_2 - d_1), & d_1 < \Delta_1 < d_2 \\ i/f, & \Delta_1 > d_2 \end{cases} \quad (20)$$

where i is the electric current flow out of the crack face, calculated using equation (14). The flux resulting from diffusion across the faces of a closed interface is computed as

$$j_{\text{diff}}^\pm = \begin{cases} \frac{\hat{D}}{RTd_1}(\mu^\pm - \mu^\mp), & \Delta_2 < d_1 \\ \frac{\hat{D}(\Delta_1 - d_1)}{RTd_1(d_2 - d_1)}(\mu^\pm - \mu^\mp), & d_1 < \Delta_1 < d_2 \\ 0, & \Delta_1 > d_2 \end{cases} \quad (21)$$

where \hat{D} is the diffusion coefficient, and μ^\pm is the chemical potential of Li ions on the two crack faces. Setting a suitably large value for \hat{D} approximates chemical potential continuity across the faces of a closed crack.

3. Finite element implementation

The governing equations listed in the preceding section can be solved using a straightforward finite element method, which must address two issues: firstly, **elements must be designed to avoid locking**, while accounting properly for the large volume changes accompanying Li insertion; secondly, the governing equations for Li transport involve the gradients of stress, which are not available in standard finite element treatments. Locking may be avoided using a minor modification of the standard B-bar method. Two approaches can be used to incorporate the effects of stress gradients. **In one method, the equations for mechanical deformation and diffusion are solved sequentially**, with the stress gradients extracted from the deformation solution and subsequently passed to the diffusion computation. Alternatively, a mixed method

can be adopted, in which some measure of stress is included as an explicit degree of freedom in the analysis. The latter approach has the advantage that an implicit (backward-Euler) time integration scheme can be used for both the viscoplastic constitutive equation and the diffusion equation, which improves numerical stability. We will follow the latter procedure here.

To proceed, we assume that the displacement, Kirchhoff stress and concentration in the electrode $u_i^{(n)} = y_i - x_i$, $\tau_{ij}^{(n)}$, $c^{(n)}$ are known at time t . Our objective is to determine $u_i^{(n+1)} = y_i - x_i$, $\tau_{ij}^{(n+1)}$, $c^{(n+1)}$ at a slightly later time $t + \Delta t$. To account for the coupling between stress and Li diffusion, it is convenient to introduce the ‘stress potential’

$$\tilde{\mu} = -\frac{1}{2\rho_0} \frac{\partial S_{ijkl}}{\partial c} \tau_{ij} \tau_{kl} - \frac{\tau_{kk}}{3\rho_0} \frac{1}{\beta} \frac{\partial \beta}{\partial c} \quad (22)$$

as an additional degree of freedom, which must be determined at time $t + \Delta t$. Note that the total chemical potential in equation (10) can then be expressed as $\mu = RT \log(\gamma c/c_0) + \tilde{\mu}(\tau_{ij})$. The stress, concentration and stress potential must satisfy mechanical equilibrium, the diffusion equation and equation (22) at time $t + \Delta t$. These are most conveniently expressed in integral form as

$$\begin{aligned} \int_{V_0} \tau_{ij}^{(n+1)} \delta \bar{L}_{ij} dV_0 + \int_{\Gamma_0} T_\alpha e_i^\alpha (\delta v_i^+ - \delta v_i^-) = 0 \\ \int_{V_0} \frac{\partial c}{\partial t} \delta c dV_0 + \int_{V_0} \frac{D}{RT} \left(1 + \frac{c}{\gamma} \frac{\partial \gamma}{\partial c} \right) \frac{\partial c}{\partial x_j} \frac{\partial \delta c}{\partial x_j} dV_0 + \int_{V_0} \frac{cD}{RT} \frac{\partial \tilde{\mu}}{\partial x_j} \frac{\partial \delta c}{\partial x_j} dV_0 \\ + \int_{A_0} \frac{1}{\rho_0} j_n \delta c dA_0 + \int_{\Gamma_0} \frac{1}{\rho_0} (j_n^+ \delta c^+ + j_n^- \delta c_i^-) dA_0 = 0 \\ \int_{V_0} \tilde{\mu} \delta \tilde{\mu} dV_0 + \int_{V_0} \left(\frac{1}{2\rho_0} \frac{\partial S_{ijkl}}{\partial c} \tau_{ij} \tau_{kl} - \frac{\tau_{kk}}{3\rho_0} \frac{1}{\beta} \frac{\partial \beta}{\partial c} \right) \delta \tilde{\mu} dV_0 = 0 \end{aligned} \quad (23)$$

where δv_i , δc , $\delta \tilde{\mu}$ are admissible variations in displacement, concentration and stress potential, and $\delta \bar{L}_{ij}$ is a virtual velocity gradient, which must be constructed to avoid locking as described below. The integrals are taken over the reference configuration. Note that the stress τ_{ij} , interfacial tractions T_α , as well as the Li flux through the electrode/electrolyte interface j_n and crack faces j_n^\pm are all functions of displacement, concentration and stress potential.

Following the standard finite element method, we interpolate the displacement and concentration fields, at time t , and stress potential at time $t + \Delta t$ between a set of N nodal values $u_i^{a(n)}$, $c^{a(n)}$, $\tilde{\mu}^a$, and introduce nodal displacement and concentration increments Δu_i^a , Δc^a during the interval Δt . The displacement fields and their variation are interpolated as

$$u_i(\mathbf{x}) = \sum_{a=1}^N N^a(\mathbf{x}) u_i^a, \quad \delta v_i(\mathbf{x}) = \sum_{a=1}^N N^a(\mathbf{x}) \delta v_i^a \quad (24)$$

with similar expressions for concentration, displacement and concentration increments, and stress potential.

As usual, the finite element interpolation scheme allows the integrals in (23) to be evaluated element by element. In a representative volume element, we compute the deformation gradient as

$$F_{ij} = \delta_{ij} + \frac{\partial u_i}{\partial x_j} = \delta_{ij} + \sum_{a=1}^n \frac{\partial N^a}{\partial x_j} u_i^a \quad (25)$$

and the velocity gradient as

$$\delta L_{ij} = \sum_{a=1}^n \frac{\partial N^a}{\partial x_k} F_{kj}^{-1} \delta v_i^a. \quad (26)$$

A slight modification of the B-bar method [25] is used to modify the deformation gradients and concentration fields inside each element to avoid locking. We define volume averages of the Jacobian of the deformation gradient $J = \det(\mathbf{F})$ and its rate of change JL_{kk} , as well as a modified concentration, as

$$\eta = \frac{1}{V_{\text{el}}} \int_{V_{\text{el}}} J \, dV_0, \quad \dot{\eta} = \frac{1}{V_{\text{el}}} \int_{V_{\text{el}}} JL_{kk} \, dV_0, \quad \bar{c} = (1 - \omega)c + \frac{\omega}{V_{\text{el}}} \int_{V_{\text{el}}} c \, dV_0 \quad (27)$$

where ω is a numerical parameter that can be selected to optimize convergence (numerical tests suggest that $\omega = 0.02$ is a suitable value), all integrals are evaluated over the reference configuration, and V_{el} is the volume (or area, in 2D) of the element. Modified measures of deformation gradient, and a compatible velocity gradient are introduced as

$$\bar{F}_{ij} = F_{ij}(\eta/J)^{1/n}, \quad \delta \bar{L}_{ij} = \delta L_{ij} + \delta_{ij}(\delta \dot{\eta}/\eta - \delta L_{kk})/n \quad (28)$$

where $n = 2$ for a 2D (plane strain) element and $n = 3$ for a 3D element. The stress in each element is then computed using the modified deformation gradient \bar{F}_{ij} and the modified concentration \bar{c} . This ensures that all possible volumetric expansion fields produced by variations in concentration can be described exactly by an appropriate set of nodal displacements.

Substituting the element interpolation functions into equation (23) yields a set of nonlinear equations for the displacement and concentration increments Δu_i^a , Δc^a and stress potential μ^a . These may be solved using a standard Newton–Raphson iteration. For convenience, we have listed explicit expressions for the residual force vectors and consistent tangents required to implement this computation in the appendix.

In our actual implementation of this approach, we have tested all the standard isoparametric linear and quadratic finite elements to interpolate the displacement, concentration and stress potential fields in the electrode. Linear quadrilateral (in 2D) and linear hexahedral (in 3D) isoparametric elements were found to have the best performance. Linear triangular and tetrahedral elements are acceptable, but have slow convergence. Quadratic elements performed extremely poorly, resulting in ill-conditioned equation systems. It may be possible to devise elements with quadratic interpolation of displacement fields, combined with a linear interpolation of concentration and stress potential, but we have not attempted to do so here.

The boundary conditions resulting from the electrochemical reactions are enforced using plane elements (or in 2D line elements), which share nodes with the underlying solid elements, and have additional nodes for which the electric potential difference $\Delta\phi$ is a degree of freedom. Material separation is modeled using cohesive zone elements, which share nodes with the two materials adjacent to the interface, and also have additional voltage nodes to enforce boundary conditions associated with electrochemical reactions on the faces of an open crack. In our computations $\Delta\phi$ is constant, so all surface and cohesive zone elements share a single voltage node. Applying a ‘force’ to this node enables the total current drawn from the electrode to be prescribed.

4. Applications

We conclude by describing several illustrative applications. We begin with a simple test that is intended to demonstrate the accuracy, stability and convergence of the finite element method. Several recent experiments have measured the evolution of stress and electrochemical response as a thin Si film on a large, stiff substrate is lithiated in a half-cell. This is a simple 1D configuration that serves both as a simple test case, and also provides an opportunity to compare model predictions with experimental measurements.

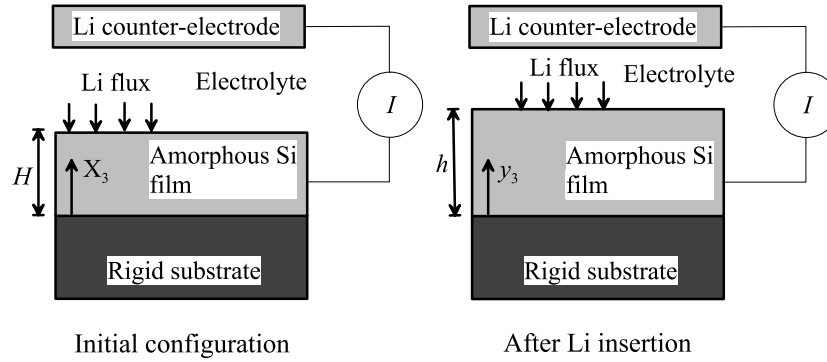


Figure 2. Schematic illustrating a thin Si film on a rigid substrate, which lithiated at a constant current density. This 1D problem is used to test the convergence and stability of the finite element method.

Table 1. Material parameter values for Si used in simulations.

Molar density of Si ρ_{0A}	$7.874 \times 10^4 \text{ mol m}^{-3}$
Mass density of Si	2.2 g cm^{-3}
Modulus of unlithiated Si electrode E_0	100 GPa
Rate of change of Si electrode modulus with concentration $\partial E / \partial c$	0
Poisson's ratio of Si electrode ν	0.26
Volumetric expansion of Si with Li concentration $(\partial \beta / \partial c)$	0.7
Characteristic strain rate for plastic flow in Si $(\dot{\epsilon}_0)$	$0.6 \times 10^{-9} \text{ s}^{-1}$
Initial yield stress of Si (σ_0)	0.12 GPa
Rate of change of flow stress in Si with concentration $(\partial \sigma_0 / \partial c)$	0.05 GPa
Stress exponent for plastic flow in Si m	4
Initial concentration of Li in Si	0.0078
Reaction rate ratio at reference concentration $\Theta(c_0)$	0.78 V
Rate of change of reaction rate ratio $\partial \Theta / \partial c$	-0.16 V
Exchange current density i_0	0.001 A m^{-2}
Symmetry factor α	0.5
Faraday constant f	96485 C mol^{-1}
Cohesive zone strength σ_{\max}	500 MPa or 125 MPa
Cohesive zone stiffness k_0	10^{20} N m^{-3}
Cohesive zone compressive stiffness k_1	10^{22} N m^{-3}
Cohesive zone length d_2	1 nm
Cohesive zone viscosity ξ	$10^{18} \text{ N s m}^{-3}$
Gas constant (R)	$8.314 \text{ J K}^{-1} \text{ mol}^{-1}$
Temperature (T)	298 K

To this end, we consider a thin-film Si electrode with uniform initial thickness H that is bonded to a rigid substrate, shown in figure 2. We assume that the film is amorphous even before lithiation, so as to avoid the need to model phase transitions or amorphization observed in crystalline Si [26]. Parameter values for amorphous Si were estimated in [22] from measurements of stress evolution in a thin-film half-cell [20], and are listed in table 1. The activity coefficient of Li in Si was taken to be unity for simplicity, but recent experiments suggest this is not a good assumption [27]. The surface of the film is lithiated by drawing a prescribed cyclic current $I(t)$ from the electrode through an external circuit (connected also to the counter-electrode, which is taken to be Li). Initially, we assume that the film does not fracture. It may, however, deform plastically. Our objective is to compute the variations of concentration, stress, plastic strain and displacement through the thickness of the film

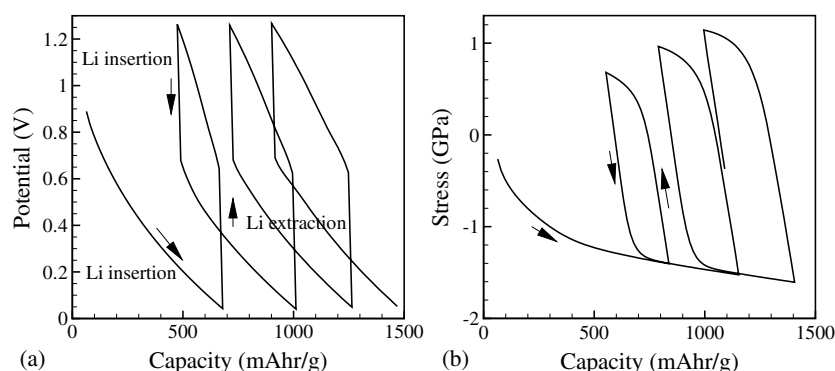


Figure 3. Predicted cycles of (a) potential and (b) average through-thickness nominal stress for a 200 nm thick amorphous Si thin-film electrode (with Li counter-electrode) subjected to cyclic lithiation at a constant current. Computations do not account for fracture in the film.

as functions of time. In addition, the computations predict the average stress components and the externally applied potential to the film, which may be compared with experimental measurements. To this end, we have obtained finite element solutions by meshing the film in the through-thickness direction with a vertical stack of linear hexahedral or linear tetrahedral elements. Symmetry boundary conditions were applied on the sides of the stack, while all displacement components are constrained at the base. Square surface elements were used to enforce the boundary conditions associated with the Butler–Volmer equation, as described in sections 2.2 and 3.

Figures 3 and 4 show a representative set of results, for a 200 nm thick film that is subjected to a cycle of lithiation and de-lithiation at a current density of 0.012 A m^{-2} . The diffusion coefficient for Li in Si is not known precisely. We have used a value of $3 \times 10^{-19} \text{ m}^2 \text{ s}^{-1}$, and with this value Li diffusion is sufficiently slow that significant gradients in concentration and stress develop in the film. Figure 3 shows the predicted cycle of electrode potential (relative to the Li counter-electrode) and average through-thickness nominal stress in the film, while figure 4 shows the time history of concentration, nominal in-plane biaxial stress and accumulated plastic strain in the film. The results in figures 3 and 4 were obtained with a mesh consisting of 100 linear hexahedral elements. The numerical parameter defined in equation (27) was set to $\omega = 0.02$, and a time step of 200 s was used.

This simple one-dimensional problem can be used to investigate the convergence of the finite element solution as the mesh and time step are refined. To this end, figure 5 shows the predicted variation of concentration and stress through the film thickness at time $t = 8000 \text{ s}$, for several mesh densities. A relatively coarse mesh, with only 24 elements through the film thickness, predicts concentration and stress variations that are within 5% of the result with 100 elements. The parameter ω must be selected carefully to yield accurate results, however. The effects of varying ω are illustrated in figure 6: for ω too small, locking behavior is observed in regions with high concentration gradients, causing very poor convergence, while large values of ω result in a form of hourglassing.

Next, we extend our computations to account for fracture in the film. Experiments show that Si films tend to develop an approximately periodic set of mutually perpendicular through-thickness cracks after cyclic lithiation. To model this failure mechanism, we construct a finite element model of a representative area element of the film, as shown in figure 6. Potential fracture nucleation sites are represented using cohesive zones which lie perpendicular to the plane of the film. Symmetry boundary conditions are applied to the edges of the simulation

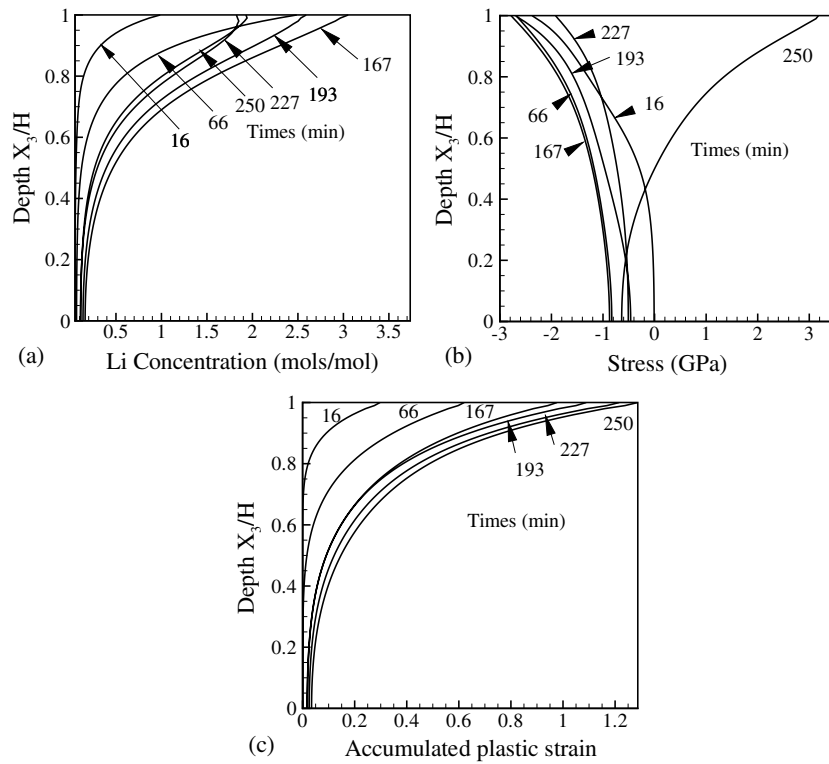


Figure 4. Predicted through-thickness variation of (a) Li concentration, (b) nominal stress and (c) accumulated plastic strain for a thin-film amorphous Si electrode.

cell, and the base of the film is assumed to be bonded to a rigid substrate. Material parameter values for the film and cohesive zone are listed in table 1. In this computation, the diffusion coefficient in Si was set to $D = 10^{-13} \text{ m}^2 \text{ s}^{-1}$. The predicted deformation and fracture in the film is illustrated in figure 7, which shows the history of deformation and fracture in the film, together with contours of the in-plane nominal stress component $J\sigma_{11} = J\sigma_{22}$. The corresponding history of average nominal stress, and the externally applied potential are plotted as functions of capacity in figure 8. During the initial lithiation cycle, the film develops a large compressive stress, which causes the film to deform plastically. When the current is reversed, the stress turns tensile, and eventually reaches the cohesive strength of the film. At this point cracks nucleate in the film, leading to a sudden drop in stress, and a corresponding small drop in the electric potential caused partly by the drop in stress, and partly by increase in surface area (and a corresponding decrease in current density). Very large crack opening displacements develop as Li is removed from the film. When the current is reversed, the cracks close, leading to a large increase in average stress in the film. Over subsequent cycles, the cracks continue to open and close. Further extensions of this model would be required to accurately characterize the behavior of thin films: for example, experiments suggest that significant deformation occurs in the current collector below the film, and that films whose thickness exceeds a critical value tend to delaminate from the substrate [28, 29]. These processes could be modeled using standard finite element methods.

Thin solid films evidently develop large stresses during lithiation, which lead to plastic flow and fracture. Consequently, such films are rarely used as electrodes. In most practical

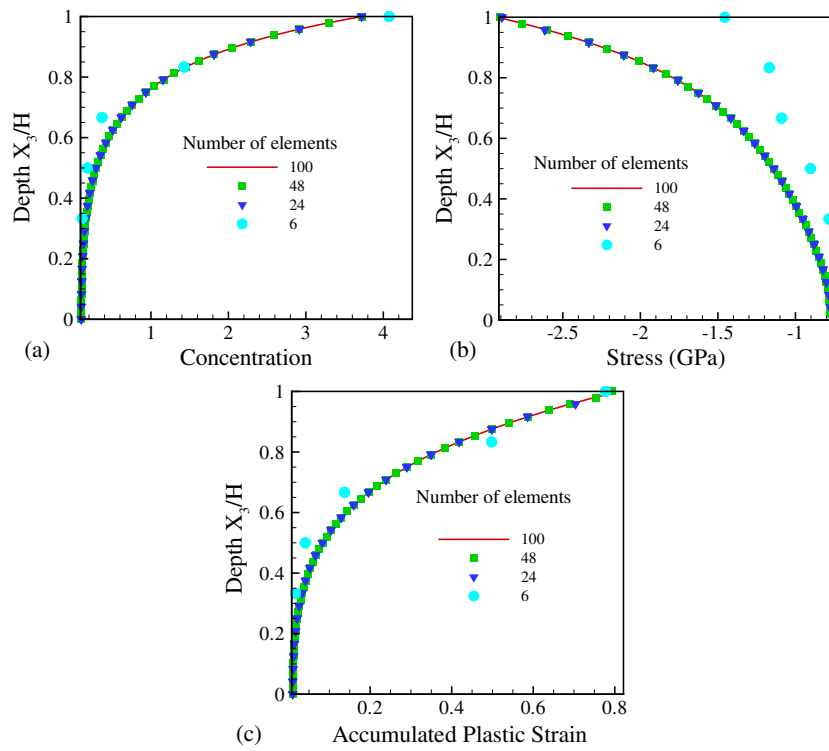


Figure 5. Predicted through-thickness variation of (a) Li concentration, (b) nominal stress and (c) accumulated plastic strain for a thin-film amorphous Si electrode at time $t = 8000$ s, for several different mesh densities through the thickness of the film. A uniform mesh was used.

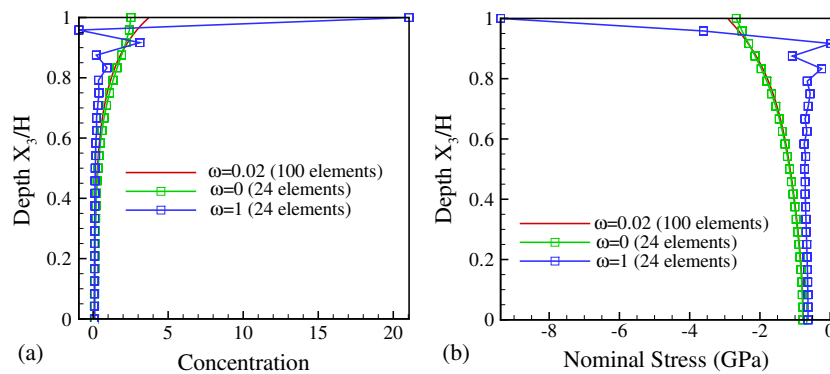


Figure 6. Predicted through-thickness variation of (a) Li concentration and (b) nominal stress for a thin-film amorphous Si electrode, for various values of the numerical parameter ω defined in equation (27). For small values of ω convergence is poor as a result of locking, for large values spurious oscillations develop in the solution as a result of 'hourglassing'.

battery materials, the electrode has a complex microstructure, consisting of particles held together by a binder. Particulate Si anodes with both micrometer-sized and nanoscale particles have shown promise [30, 31] Nevertheless, particles may deform plastically or fracture under sufficiently high charging or discharging rates. We conclude by modeling plastic flow and

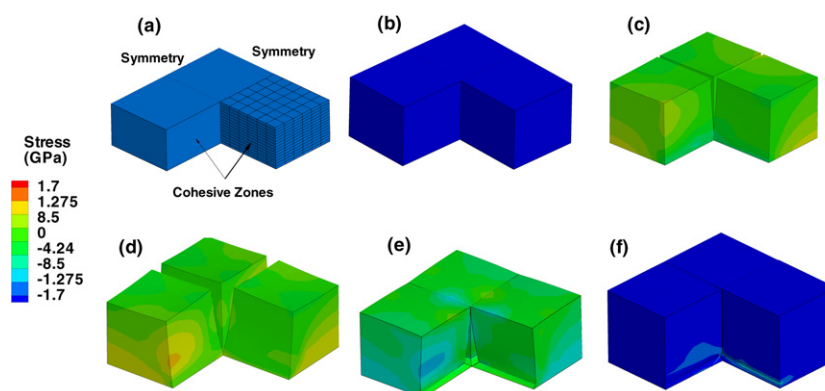


Figure 7. Fracture, deformation and stress in a thin-film amorphous Si electrode during cyclic lithiation at a constant current. The contours show distributions of nominal stress acting perpendicular to the fracture planes. Figure 8 shows the potential and average through-thickness stress for each configuration labeled (a)–(f). Three unit cells are shown for visualization purposes but in actual simulations only the meshed region in (a) was modeled.

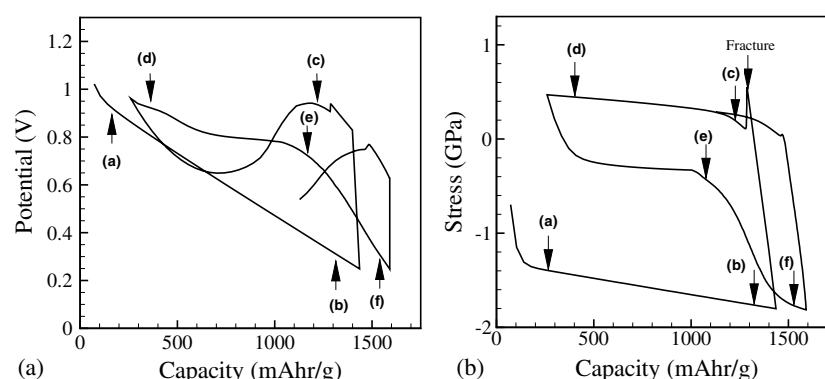


Figure 8. Predicted cycles of potential and average through-thickness nominal stress for a 200 nm thick amorphous Si thin-film electrode (with Li counter-electrode) subjected to cyclic lithiation at a constant current. Computations account for fracture in the film. The configuration of the film at instants (a)–(f) is shown in figure 7.

fracture in a model microstructure consisting of an array of connected particles, illustrated in figures 9 and 10. The particles are spherical, with a $10\ \mu\text{m}$ diameter. The particles are arranged in a periodic rectangular array, with spacing $8.4\ \mu\text{m}$, so that neighboring particles are connected by circular necks. Large stresses act on the regions connecting neighboring particles, so these are potential locations for fracture. Accordingly, the connections between neighboring particles are modeled using the cohesive zone described in section 2.3. Material parameter values for the particles are listed in table 1, except that the exchange current density was increased to $0.01\ \text{A m}^{-2}$ for this computation. The diffusion coefficient was taken to be $10^{-15}\ \text{m}^2\ \text{s}^{-1}$. The particles are lithiated through their exposed surfaces by applying a constant external current of $52.7 \times 10^3\ \text{A m}^{-3}$ to the unit cell. The unit cell was allowed to expand freely in all three directions (with appropriate symmetry boundary conditions), so that the average stress in the microstructure remains zero. The corresponding potential–capacity curve is shown in figure 11.

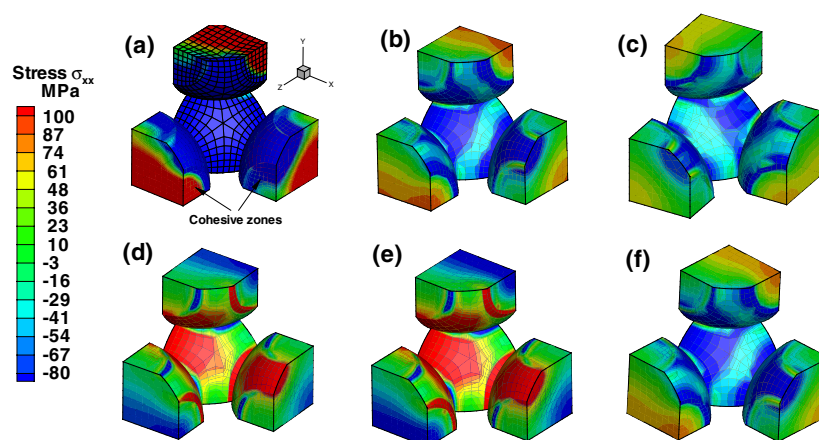


Figure 9. Variation of stress in a model porous electrode consisting of spherical particles connected by a circular neck. The interfaces between neighboring particles have a cohesive strength of 500 MPa, which prevents fracture. The contours show the Kirchhoff stress component acting parallel to the x direction. Labels (a)–(f) correspond to those shown in the voltage–capacity curve in figure 11.

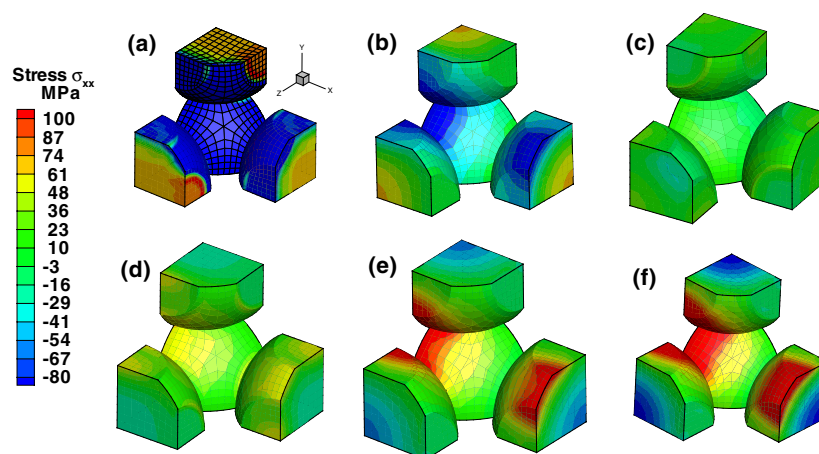


Figure 10. Variation of stress in a model porous electrode consisting of spherical particles connected by a circular neck. The contours show the Kirchhoff stress component acting parallel to the x direction. The interfaces between neighboring particles have a cohesive strength of 125 MPa, which causes the neck between particles to fracture. A crack has initiated in (A), and the connection is severed completely at (D). Labels (A)–(F) correspond to those shown in the voltage–capacity curve in figure 11.

A complex local stress distribution develops in the particles, as shown in figures 9 and 10. During lithiation, the exterior surface of the particles develops a compressive stress, which is sufficient to cause some plastic flow near the surface during the first few minutes of charging. The particles deform elastically during the rest of the charge–discharge cycle. A large tensile stress also develops near the center of the necks between particles during the first few minutes of lithiation: for the simulation in which the necks have a cohesive strength of only 125 MPa (figure 10) this stress nucleates a crack. Crack nucleation relaxes stresses, and consequently

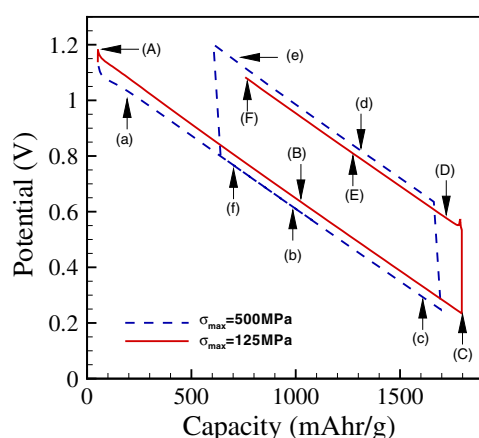


Figure 11. Variation of externally applied potential with capacity for the porous electrode microstructures illustrated in figures 9 and 10. Labels (a)–(f) and (A)–(F) correspond to those shown in figures 9 and 10.

results in a small increase in the electrode potential, as shown in figure 11. At this stage the necks between particles are subjected to compressive stress at the outer edge of the necks (as required for equilibrium), so that the cracks do not sever the links between neighboring particles. Full fracture occurs when the current is reversed, and the exterior of the particles develops tensile stress. A small drop in potential can be observed in figure 11 (just before label D) at the instant of full fracture, caused by the increase in surface area available for lithiation. Once the particles are fully separated, a current path may not be present between the electrode particles and the current collector, which would cause full failure of this region of the battery microstructure. Our model does not directly model current flow through the solid particles, but it would be straightforward to extend the model to include this process, as well as a realistic model of the electrolyte.

5. Conclusions

A simple finite element procedure has been described that is capable of modeling the coupled processes of diffusion, deformation and fracture in representative Li ion battery electrode microstructures. A simple mixed finite element allows the governing equations for diffusion and equilibrium to be fully coupled, so that a fully implicit time integration scheme can be used. Large volume changes can be modeled using a minor extension of the standard B-bar method [25]. In addition, surface and cohesive zone elements can be used to model Li insertion at the electrode surfaces and crack nucleation and propagation. Numerical tests suggest that the procedure is stable and convergent, and shows promise in modeling the complex processes of deformation and failure in 3D electrode microstructures. Future extensions of the approach will need to address coupling the model of the solid electrode to existing models of the fluid electrolyte, and to account for the effects of fracture on electric current flow through the solid electrode.

Acknowledgment

The authors are grateful for support from the US Department of Energy through DOE EPSCor Implementation Grant No DE-SC0007074.

Appendix

As an aid to readers who wish to implement the finite element method outlined in section 3, we list explicit expressions for the residual force vectors and consistent tangents for the Newton–Raphson iteration. **A lengthy but straightforward calculation yields the following system of linear equations for the corrections** du_k^b , dc^b and $d\mu^b$ to the approximations to Δu_i^a , Δc^a and μ^a at a generic increment:

$$\begin{aligned} K_{aibk}^{uu} du_k^b + K_{aib}^{uc} dc^b &= -R_i^{ua} \\ K_{ab}^{cc} dc^b + K_{ab}^{c\mu} d\mu^b + K_{abk}^{cu} du_k^b &= -R^{ca} \\ K_{ab}^{\mu\mu} d\mu^b + K_{ab}^{\mu c} dc^b + K_{abk}^{\mu u} du_k^b &= -R^{\mu a} \end{aligned} \quad (29)$$

where the residual force vectors are given by

$$\begin{aligned} R_{ia}^u &= \int_{V_0} \tau_{ij} [\Delta \bar{F}_{kl}, \bar{c}] \frac{\partial N^a}{\partial y_j} + \frac{\tau_{pp} [\bar{F}_{kl}, \bar{c}]}{n} \left(\frac{1}{\eta} \frac{\partial \eta}{\partial u_i^a} - \frac{\partial N^a}{\partial y_i} \right) dV_0 + \int_{\Gamma_0} T_\alpha e_i^\alpha (N^{a+} - N^{a-}) dA \\ R_{ia}^c &= \int_{V_0} \frac{\Delta c}{\Delta t} N^a dV_0 + \int_{V_0} \frac{D}{RT} \left(\frac{\partial c}{\partial x_j} + \frac{c}{\gamma} \frac{\partial \gamma}{\partial c} \right) \frac{\partial N^a}{\partial x_j} dV_0 + \int_{V_0} \frac{cD}{RT} \frac{\partial \tilde{\mu}}{\partial x_j} \frac{\partial N^a}{\partial x_j} dV_0 \\ &\quad + \int_{A_0} j_n N^a dA_0 + \int_{\Gamma_0} (j_n^+ N^{a+} + j_n^- N^{a-}) dA_0 \\ R^{\mu a} &= \int_{V_0} \left(\mu_A + \frac{1}{2\rho_{0A}} \frac{\partial S_{ijkl}}{\partial c} \tau_{ij} \tau_{kl} + \frac{\tau_{kk}}{3\rho_{0A}} \frac{1}{\beta} \frac{\partial \beta}{\partial c} N^a \right) dV_0 \end{aligned} \quad (30)$$

where $S_{ijkl}(c)$, β and $\partial\beta/\partial c$ are evaluated using the concentration at time t , and where

$$\frac{\partial \eta}{\partial u_i^a} = \frac{1}{V_{el}} \int_{V_{el}} J \frac{\partial N^a}{\partial y_i} dV, \quad \frac{\partial N^a}{\partial y_i} = \frac{\partial N^a}{\partial x_k} F_{ki}^{-1}. \quad (31)$$

The consistent tangents are

$$\begin{aligned} K_{aibk}^{uu} &= \int_{V_0} C_{mjpr}^{ep} \left(\frac{\partial N^b}{\partial \bar{y}_r} \delta_{pk} + \frac{\delta_{pr}}{n} \left(\frac{1}{\eta} \frac{\partial \eta}{\partial u_k^b} - \frac{\partial N^b}{\partial y_k} \right) \right) \left(\delta_{im} \frac{\partial N^a}{\partial y_j} + \frac{\delta_{mj}}{n} \left(\frac{1}{\eta} \frac{\partial \eta}{\partial u_i^a} - \frac{\partial N^a}{\partial y_i} \right) \right) dV_0 \\ &\quad + \int_{V_0} \left\{ -\tau_{ij} \frac{\partial N^a}{\partial y_k} \frac{\partial N^b}{\partial y_j} + \frac{\tau_{kk}}{n} \left(\frac{1}{\eta} \frac{\partial^2 \eta}{\partial u_i^a \partial u_k^b} - \frac{1}{\eta^2} \frac{\partial \eta}{\partial u_i^a} \frac{\partial \eta}{\partial u_k^b} + \frac{\partial N^a}{\partial y_k} \frac{\partial N^b}{\partial y_i} \right) \right\} dV_0 \\ &\quad + \int_{\Gamma_0} \frac{\partial T_\alpha}{\partial \Delta \beta} e_k^\beta e_i^\alpha (N^{b+} - N^{b-}) (N^{a+} - N^{a-}) dA \end{aligned} \quad (32)$$

$$K_{aib}^{uc} = \int_{V_0} \frac{\partial \tau_{mj}}{\partial \Delta c} ((1 - \omega) N^b + \omega \bar{N}^b) \left(\delta_{im} \frac{\partial N^a}{\partial y_j} + \frac{\delta_{mj}}{n} \left(\frac{1}{\eta} \frac{\partial \eta}{\partial u_i^a} - \frac{\partial N^a}{\partial y_i} \right) \right) dV_0 \quad (33)$$

$$\begin{aligned} K_{ab}^{cc} &= \int_{V_0} \frac{1}{\Delta t} N^b N^a + \int_{V_0} \frac{D}{RT} \left(\left[1 + \frac{c}{\gamma} \frac{\partial \gamma}{\partial c} \right] \frac{\partial N^b}{\partial x_j} + \frac{\partial}{\partial c} \left[\frac{c}{\gamma} \frac{\partial \gamma}{\partial c} \right] N^b \frac{\partial c}{\partial x_j} + N^b \frac{\partial \tilde{\mu}}{\partial x_j} \right) \frac{\partial N^a}{\partial x_j} dV_0 \\ &\quad + \int_{A_0} \frac{\partial j_n}{\partial c} N^b N^a dA_0 + \int_{\Gamma_0} \left(\left[\frac{\partial j_n^+}{\partial c^+} N^{b+} + \frac{\partial j_n^+}{\partial c^-} N^{b-} \right] N^{a+} \right. \\ &\quad \left. + \left[\frac{\partial j_n^-}{\partial c^+} N^{b+} + \frac{\partial j_n^-}{\partial c^-} N^{b-} \right] N^{a-} \right) dA_0 \end{aligned} \quad (34)$$

$$K_{abk}^{cu} = \int_{\Gamma_0} \left(\frac{\partial j_n^+}{\partial \Delta_1} e_k^1 N^{b+} N^{a+} + \frac{\partial j_n^-}{\partial \Delta_1} e_k^1 N^{b-} N^{a-} \right) dA_0 \quad (35)$$

$$K_{ab}^{c\mu} = \int_{V_0} \frac{cD}{RT} \frac{\partial N^b}{\partial x_j} \frac{\partial N^a}{\partial x_j} dV_0 + \int_{A_0} \frac{\partial j_n}{\partial \mu} N^b N^a dA_0 \\ + \int_{\Gamma_0} \left(\left[\frac{\partial j_n^+}{\partial \mu^+} N^{b+} + \frac{\partial j_n^+}{\partial \mu^-} N^{b-} \right] N^{a+} + \left[\frac{\partial j_n^-}{\partial \mu^+} N^{b+} + \frac{\partial j_n^-}{\partial \mu^-} N^{b-} \right] N_i^{a-} \right) dA_0 \quad (36)$$

$$K_{ab}^{\mu\mu} = \int_V N^b N^a dV \quad (37)$$

$$K_{ab}^{\mu c} = \int_V \left(\frac{1}{\rho_{0A}} \frac{\partial S_{ijkl}}{\partial c} \frac{\partial \tau_{ij}}{\partial c} \tau_{kl} + \frac{1}{3\rho_{0A}} \frac{\partial \tau_{kk}}{\partial c} \frac{1}{\beta} \frac{\partial \beta}{\partial c} \right) ((1-\omega)N^b + \omega\bar{N}^b) N^a dV \quad (38)$$

$$K_{abk}^{\mu u} = \int_V \left(\frac{1}{\rho_{0A}} \frac{\partial S_{ijmn}}{\partial c} C_{ijpr}^{ep} \tau_{mn} + \frac{1}{3\rho_{0A}} C_{jjpr}^{ep} \frac{1}{\beta} \frac{\partial \beta}{\partial c} \right) \\ \times \left(\frac{\partial N^b}{\partial \bar{y}_r} \delta_{pk} + \frac{\delta_{pr}}{n} \left(\frac{1}{\eta} \frac{\partial \eta}{\partial w_k^b} - \frac{\partial N^b}{\partial y_k} \right) \right) N^a dV \quad (39)$$

In these expressions, we have defined

$$\bar{N}^a = \frac{1}{V_{el}} \int_{V_{el}} N^a dV, \quad \frac{\partial N^a}{\partial \bar{y}_i} = \frac{\partial N^a}{\partial x_k} \bar{F}_{ki}^{-1} \\ \frac{\partial^2 \eta}{\partial u_k^b \partial u_i^a} = \frac{1}{V_{el}} \int_{V_{el}} \left(J \frac{\partial N^b}{\partial y_k} \frac{\partial N^a}{\partial y_i} - J \frac{\partial N^a}{\partial y_k} \frac{\partial N^b}{\partial y_i} \right) dV. \quad (40)$$

The stress τ_{ij} and material tangents C_{ijkl}^{ep} are computed using the usual fully implicit time integration scheme. The stress state $\tau_{ij}^{(n)}$ and deformation gradient $\bar{F}_{ij}^{(n)}$ at time t , and the deformation gradient increment $\Delta \bar{F}_{ij} = \bar{F}_{ij}^{(n+1)} - \bar{F}_{ij}^{(n)}$ are known. To compute the stress $\tau_{ij}^{(n+1)}$ at time $t + \Delta t$, we begin by computing the strain and rotation increments

$$\Delta \varepsilon_{ij} = \frac{1}{2} (\Delta \bar{F}_{ik} \bar{F}_{kj}^{-1} + \Delta \bar{F}_{jk} \bar{F}_{ki}^{-1}), \quad \Delta R_{ij} = \frac{1}{2} (\Delta \bar{F}_{ik} \bar{F}_{kj}^{-1} - \Delta \bar{F}_{jk} \bar{F}_{ki}^{-1}). \quad (41)$$

Next, compute the deviatoric strain increment and deviatoric stress at time t ,

$$\Delta e_{ij} = \Delta \varepsilon_{ij} - \Delta \varepsilon_{kk} \delta_{ij} / 3, \quad \tau_{ij}^{D(n)} = \tau_{ij}^{(n)} - \tau_{kk}^{(n)} \delta_{ij} / 3. \quad (42)$$

The deviatoric stress in the absence of plastic flow follows as

$$\tau_{ij}^* = \tau_{ij}^{D(n)} + \frac{E}{1+\nu} \Delta e_{ij} + \tau_{ik}^{D(n)} \Delta R_{kj} - \Delta R_{ik} \tau_{kj}^{D(n)} + \frac{1}{E} \frac{\partial E}{\partial c} \tau_{ij}^{D(n)} \Delta c. \quad (43)$$

If the effective von Mises elastic stress $\tau_e^* = \sqrt{3\tau_{ij}^* \tau_{ij}^*} / 2 < \sigma_0$ the plastic strain increment is zero. Otherwise, the effective plastic strain increment $\Delta \varepsilon_e$ must be computed by solving the following nonlinear equation:

$$0 = \frac{\tau_e^*}{\sigma_0} - 1 - \frac{3E}{2\sigma_0(1+\nu)} \Delta \varepsilon_e - \left(\frac{\Delta \varepsilon_e}{\varepsilon_0 \Delta t} \right)^{1/m}. \quad (44)$$

The updated stress then follows as

$$\tau_{ij}^{(n+1)} = \left(1 - \frac{3E}{2(1+\nu)\tau_e^*} \Delta \varepsilon_e \right) \tau_{ij}^* + \tau_{kk}^{(n)} \frac{\delta_{ij}}{3} + \frac{E}{3(1-2\nu)} \left(\Delta \varepsilon_{kk} - \frac{1}{\beta} \frac{\partial \beta}{\partial c} \Delta c \right) \\ + \frac{1}{3E} \frac{\partial E}{\partial c} \tau_{kk}^{(n)} \Delta c. \quad (45)$$

Finally, the material tangents are

$$C_{mjpr}^{ep} = \frac{\partial \tau_{mj}}{\partial \Delta \varepsilon_{pr}} + \frac{1}{2} (\tau_{mp}^{(n)} \delta_{jr} + \tau_{pj}^{(n)} \delta_{mr} - \tau_{mr}^{(n)} \delta_{jp} - \delta_{mp} \tau_{rj}^{(n)})$$

$$\frac{\partial \tau_{ij}}{\partial \Delta \varepsilon_{kl}} = \frac{\lambda E}{1 + \nu} \left(\frac{1}{2} (\delta_{ik} \delta_{jl} + \delta_{jk} \delta_{il}) - \frac{1}{3} \delta_{ij} \delta_{kl} + \frac{9E(\Delta \varepsilon_e - 1/\gamma)}{4(1 + \nu)\lambda \tau_e^*} \frac{\tau_{ij}^* \tau_{kl}^*}{\tau_e^* \tau_e^*} \right) + \frac{E}{3(1 - 2\nu)} \delta_{ij} \delta_{kl} \quad (46)$$

where

$$\lambda = 1 - \frac{3E}{2(1 + \nu)\tau_e^*} \Delta \varepsilon_e, \quad \gamma = \left(\frac{3E}{2(1 + \nu)\tau_e^*} + \frac{\lambda}{m \Delta \varepsilon_e} \right) \quad (47)$$

and

$$\frac{\partial \tau_{ij}^{n+1}}{\partial \Delta c} = \frac{\partial \lambda}{\partial c} \tau_{ij}^* + \lambda \frac{1}{E} \frac{\partial E}{\partial c} \tau_{ij}^{(n)} - \frac{E}{3(1 - 2\nu)} \frac{1}{\beta} \frac{\partial \beta}{\partial c} \delta_{ij} \quad (48)$$

where

$$\frac{\partial \lambda}{\partial c} = \frac{9}{4(1 + \nu)} \left\{ \frac{\Delta \varepsilon_e}{\tau_e^*} - \left(\frac{3E}{2\sigma_0(1 + \nu)} + \frac{1}{m \Delta \varepsilon_e} \left(\frac{\Delta \varepsilon_e}{\dot{\varepsilon}_0 \Delta t} \right)^{1/m} \right)^{-1} \frac{1}{\sigma_0} \right\} \frac{\partial E}{\partial c} \frac{\tau_{ij}^{D*} \tau_{ij}^{D(n)}}{\tau_e^{*2}}. \quad (49)$$

References

- [1] Vetter J, Novák P, Wagner M R, Veit C, Möller K-C, Besenhard J O, Winter M, Wohlfahrt-Mehrens M, Vogler C and Hammouche A 2005 Ageing mechanisms in lithium-ion batteries *J. Power Sources* **147** 269–81
- [2] Verbrugge M W and Cheng Y-T 2008 Stress distribution within spherical particles undergoing electrochemical insertion and extraction *Electrochem. Soc. Trans.* **16** 127–39
- [3] Verbrugge M W and Cheng Y-T 2009 Stress and strain-energy distributions within diffusion-controlled insertion-electrode particles subjected to periodic potential excitations *J. Electrochem. Soc.* **156** A927–37
- [4] Cheng Y-T and Verbrugge M W 2009 Evolution of stress within a spherical insertion electrode particle under potentiostatic and galvanostatic operation *J. Power Sources* **190** 453–60
- [5] Cheng Y-T and Verbrugge M W 2010 Diffusion-induced stress, interfacial charge transfer, and criteria for avoiding crack initiation of electrode particles *J. Electrochem. Soc.* **157** A508–16
- [6] Zhang X-C, Shyy W and Sastry A M 2007 Numerical simulation of intercalation-induced stress in Li-ion battery electrode particles *J. Electrochem. Soc.* **154** A910–6
- [7] Seo J H, Chung M, Park M, Ha S W, Zhang X and Sastry A M 2011 Generation of realistic particle structures and internal stress: a numerical/AFM study of LiMn₂O₄ particles *J. Electrochem. Soc.* **158** A434–42
- [8] Chung M D, Seo J H, Zhang X and Sastry A M 2011 Implementing realistic geometry and measured diffusion coefficients into single particle electrode modeling based on experiments with single LiMn₂O₄ spinel particles *J. Electrochem. Soc.* **158** A371–8
- [9] Park J, Lu W and Sastry A M 2011 Numerical simulation of stress evolution in lithium manganese dioxide particles due to coupled phase transition and intercalation *J. Electrochem. Soc.* **158** A201–6
- [10] Grantab R and Shenoy V B 2011 Location- and orientation-dependent progressive crack propagation in cylindrical graphite electrode particles *J. Electrochem. Soc.* **158** A948–54
- [11] Deshpande R, Cheng Y-T and Verbrugge M W 2010 Modeling diffusion-induced stress in nanowire electrode structures *J. Power Sources* **195** 5081–8
- [12] Bhandakkar T K and Gao H J 2010 Cohesive modeling of crack nucleation under diffusion induced stresses in a thin strip: implications on the critical size for flaw tolerant battery electrodes *Int. J. Solids Struct.* **47** 1424–34
- [13] Haftbaradaran H, Gao H J and Curtin W A 2010 A surface locking instability for atomic intercalation into a solid electrode *Appl. Phys. Lett.* **96** 091909
- [14] Garcia R E, Chiang Y-M, Carter W C, Limthongkul P and Bishop C M 2005 Microstructural modeling and design of rechargeable lithium-ion batteries *J. Electrochem. Soc.* **152** A255–63
- [15] Christensen J and Newman J 2006 Stress generation and fracture in lithium insertion materials *J. Solid State Electrochem.* **10** 293–319
- [16] Wang C-W and Sastry A M 2007 Mesoscale modeling of a Li-ion polymer cell *J. Electrochem. Soc.* **154** A1035–47

- [17] Christensen J 2010 Modeling diffusion-induced stress in Li-ion cells with porous electrodes *J. Electrochem. Soc.* **157** A366–80
- [18] Renganathan S, Sikha G, Santhanagopalan S and White R E 2010 Theoretical analysis of stresses in a lithium ion cell *J. Electrochem. Soc.* **157** A155–63
- [19] Golmon S, Maute K and Dunn M L 2009 Numerical modeling of electrochemical–mechanical interactions in lithium polymer batteries *Comput. Struct.* **87** 1567–79
- [20] Sethuraman V A, Srinivasan V, Bower A F and Guduru P R 2010 *In situ* measurements of stress-potential coupling in lithiated silicon *J. Electrochem. Soc.* **157** A1253–61
- [21] Zhao K, Pharr M, Vlassak J J and Suo Z 2011 Large plastic deformation in high-capacity lithium-ion batteries caused by charge and discharge *J. Am. Ceram. Soc.* **94** S226–35
- [22] Bower A F, Guduru P and Sethuraman V 2011 A Finite strain model of stress, diffusion, plastic flow and electrochemical reactions in a Li ion half-cell *J. Mech. Phys. Solids* **59** 804–28
- [23] Newman J and Thomas-Alyea K E 2004 *Electrochemical Systems* 3rd edn (New York: Wiley-Interscience)
- [24] Ortiz M and Pandolfi A 1999 Finite-deformation irreversible cohesive elements for three-dimensional crack propagation analysis *Int. J. Numer. Methods Eng.* **44** 1267–82
- [25] Simo J and Hughes T J R 1998 *Computational Inelasticity* (Berlin: Springer)
- [26] Limthongkul P, Jang Y-I, Dudney N J and Chiang Y-M 2003 Electrochemically-driven solid-state amorphization in lithium–silicon alloys and implications for lithium storage *Acta Mater.* **51** 1103–13
- [27] Sheldon B W, Soni S K, Xiao X and Qi Y 2012 Stress contributions to solution thermodynamics in Li–Si alloys *Electrochem. Solid State Lett.* **15** A9–11
- [28] Chon M J, Sethuraman V A, McCormick A, Srinivasan V and Guduru P R 2011 Real-time measurement of stress and damage evolution during initial lithiation of crystalline silicon *Phys. Rev. Lett.* **107** 045503
- [29] Xiao X, Liu P, Verbrugge M W, Haftbaradaran H and Gao H 2011 Improved cycling stability of silicon thin film electrodes through patterning for high energy density lithium batteries *J. Power Sources* **196** 1409–16
- [30] Obrovac M N and Krause L J 2007 Reversible cycling of crystalline silicon powder *J. Electrochem. Soc.* **154** A103–8
- [31] Magasinski A, Dixon P, Hertzberg B, Kvit A, Ayala J and Yushin G 2010 High-performance lithium-ion anodes using a hierarchical bottom-up approach *Nature Mater.* **9** 353–8